LA-UR- 09-03970

Approved for public release; distribution is unlimited.

Title: Tomographic Imaging with Soft Cosmic Rays

Author(s):
Leticia Cuellar
Konstantin Borozdin
Andrew Green
Nicolas Hengartner
Christopher Morris
Larry Schultz

Intended for: Department of Homeland Security

Los Alamos
NATIONAL LABORATORY
EST. 1943

Los Alamos National Laboratory, an affirmative action/equal opportunity employer, is operated by the Los Alamos National Security, LLC for the National Nuclear Security Administration of the U.S. Department of Energy under contract DE-AC52-06NA25396. By acceptance of this article, the publisher recognizes that the U.S. Government retains a nonexclusive, royalty-free license to publish or reproduce the published form of this contribution, or to allow others to do so, for U.S. Government purposes. Los Alamos National Laboratory requests that the publisher identify this article as work performed under the auspices of the U.S. Department of Energy. Los Alamos National Laboratory strongly supports academic freedom and a researcher's right to publish; as an institution, however, the Laboratory does not endorse the viewpoint of a publication or guarantee its technical correctness.

Form 836 (7/06)

Tomographic Imaging with Soft Cosmic Rays

Leticia Cuéllar, Konstantin Borozdin, Andrew Green,
Nicolas Hengartner, Christopher Morris and Larry Schultz
Los Alamos National Laboratory
email: {leticia, kbor, a_green, nick, cmorris, schultz}@lanl.gov

June 15, 2009

1 Introduction

Muons are highly energetic charged particles produced by decaying pions in the upper atmosphere. They travel at near relativistic speed and have the ability to traverse significant amount of matter. The induced scattering from the Coulomb interaction of matter and muons has been exploited in passive imaging of high-Z materials. But not all muons scatter. Lower energetic particles can be stopped. These stopped particles provide information about the lower Z materials.

This report investigates the feasibility of doing image reconstruction, and the ability to distinguish among low and medium Z-density materials using the information about stopped particles. We develop an algorithm using maximum likelihood to estimate the stopping density of different materials, and test it on Geant 4 simulations and some simplified versions thereof . This research is motivated by the ultimate goal of developing the capability of detecting explosives in light rail mass transit.

The material is organized as follows: Section 2 describes the problem and uses maximum likelihood to solve it. Sections 3 presents results of simulations performed assuming the particles have exponential energy distribution, section 4 investigates the particles energy distribution used in Geant 4, section 5 shows results of simulations using this energy distribution, and section 6 does tomographic image reconstruction for Geant 4 simulations. We conclude in section 7.

2 Soft Cosmic Tomographic Image Reconstruction using Maximum Likelihood

We investigate the feasibility of doing tomographic image reconstruction using soft cosmic rays. Section 2.1 describes the preliminaries of the probelm, section 2.2 computes the likelihood function, sections 2.3 explores the feasibility of using the Expection-Maximization algorithm (EM) used successfully in [6] and [7], section 2.4 presents the direct optimization of the likelihood function and we conclude discussing some implementation details.

2.1 Preliminaries

A muon with energy E enters a volume of interest along a path γ. It is stopped in the volume if the resistance along the path γ exceeds the energy, that is

$$R_\gamma = \int \rho(\gamma(s))ds > E,$$

where $\rho(\cdot)$ is the stopping density. Define the indicator variable

$$Z = \begin{cases} 0 & \text{muon is stopped in the volume} \\ 1 & \text{muon passes through the volume} \end{cases}$$

and assume that the energy E of the muon, that is unobserved, has cummulative probability distribution H. It follows that the probability that a randomly chosen muon traverses the volume along the path γ is

$$\begin{aligned} \mathbb{P}[Z=1|\gamma] &= \int \mathbb{P}[Z=1|\gamma,E]H(dE) \\ &= \int \mathbb{I}\{E > \int \rho(\gamma(s))ds\}H(dE) \\ &= 1 - H\left(\int \rho(\gamma(s))ds\right). \end{aligned} \tag{1}$$

2.2 Likelihood

For ease of exposition, let us consider a layered two-dimensional *volume* shown in figure 1. The stopping density in each of the m layers is constant. Let ℓ_{kj} denote the length of the path of the kth muon in the jth layer (with the convention that we index from top to bottom), and collect all these lengths into the vector

$$L_k = (\ell_{k1}, \ell_{k2}, \ldots, \ell_{km}).$$

We can then rewrite the probability of stopping (1) as

$$\mathbb{P}[Z=1|\gamma] = 1H(L_k^t\rho),$$

where $\rho = (\rho_1, \ldots, \rho_m)$ is the true vector of stopping densities in each layer. Given data $(\gamma_1, Z_1), \ldots, (\gamma_n, Z_n)$, we can calculate the likelihood to be

$$\mathscr{L}(\rho) = \prod_{k=1}^{n} (1 - H(L_k^t\rho))^{Z_k} H(L_k^t\rho)^{1-Z_k}, \tag{2}$$

and a statistical tomographic reconstruction can be obtained by maximizing the likelihood with respect to the parameter ρ. There are many numerical approaches to operate this optization. The challenge is to device algorithms that suitably scale with the number of layers[1].

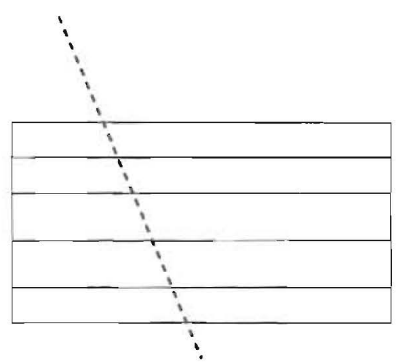

Figure 1: Layered volume.

By analogy with the tomographic image reconstruction from scattered muons, we consider an application of the Expectation-Maximization (E-M) algorithm. In later sections, we shall discuss other numerical algorithms for maximizing the likelihood.

[1] In real applications, we will *voxilize* the volume into N voxels. Let $L_{i,j}$ be the length of the path partilcle i traverses through voxel j. Within each voxel j, we assume the stopping density ρ_j to be constant, Then for $\rho = (\rho_1, \ldots, \rho_N) \in \mathbb{R}^N$,

2.3 The E-M algorithm

Several people have suggested the Expectation-Maximization (E-M) framework to optimize the likelihood (2). To do this, let us introduce the (unobserved) auxilliary variables $\xi_1, \xi_2, \ldots, \xi_m$ that describe the events that a particular muon traverses each of the m layers, that is

$$\xi_j = \begin{cases} 1 & \text{muon traverses } j^{th} \text{ layer} \\ 0 & \text{muon is stopped in } j^{th} \text{ layer} \\ -1 & \text{muon does not enter the } j^{th} \text{ layer} \end{cases}.$$

Remark that the value -1 is introduced to ensure that these random variables are well defined. Next, observe that the indicator Z_k that the kth muon traverses the volume can be written in terms of these unobserved random variables $(\xi_{k1}, \ldots, \xi_{km})$ as

$$Z_k = \prod_{j=1}^{m} \xi_{kj}.$$

The E-M algorithm starts with an inital guess $\rho^{(0)}$ for the stopping density and iteratively computes the conditionally expected loglikelihood of the full data given the observed data

$$Q(\rho||\rho^{(r)}) = \sum_{k=1}^{n} \mathbb{E}_{\rho^{(r)}} \left[\log \left(\mathbb{P}_{\rho^{(r)}}[\xi_{k1}, \ldots, \xi_{km}, Z_k] \right) \middle| Z_k \right]$$

and iteratively find its maximizer

$$\rho^{(r+1)} = \arg\max Q(\rho||\rho^{(r)}).$$

2.3.1 The expectation step

Let us focus on evaluating the conditional expectation

$$\mathbb{E}_{\rho^{(r)}} \left[\log \left(\mathbb{P}_{\rho^{(r)}}[\xi_{k1}, \ldots, \xi_{km}, Z_k] \right) \middle| Z_k \right].$$

For $Z_k = 1$, it follows that $\xi_{k1} = \xi_{k2} = \cdots = \xi_{km} = 1$, and hence

$$\mathbb{P}[\xi_{k1}, \ldots, \xi_{km}, Z_k = 1] = 1 - H(L_k^t \rho).$$

---

we can write the resistance along the path of the ith particle γ_i as

$$R_{\gamma_{i,j}} = L_i^t \rho$$

to conclude that the probability that it traverse the volume is

$$\mathbf{P}(Z_i = 1) = 1 - H(L_i^t \rho).$$

The loglikelihood function of the data is

$$\mathscr{L}(\rho) = \sum_{i=1}^{M} Z_i \log(1 - H(L_i^t \rho)) + (1 - Z_i) \log H(L_i^t \rho), \tag{3}$$

where M is the number of incident particles. The problem then is to find ρ that maximizes $\mathscr{L}$.

Hence

$$\begin{aligned}\mathbb{E}_{\rho^{(r)}}\left[\log\left(\mathbb{P}_{\rho^{(r)}}[\xi_{k1},\ldots,\xi_{km},Z_k]\right)\middle|Z_k=1\right] &= \log\left(1-H(L_k^t\rho)\right)\mathbb{P}_{\rho^{(r)}}[\xi_{k1}=\cdots=\xi_{km}=1|Z_k=1]\\ &= \log\left(1-H(L_k^t\rho)\right).\end{aligned}$$

When $Z_k=0$, either one of the following m disjoint events occur:

$$\begin{array}{ll} A_1 & \xi_{k1}=0,\xi_{k2}=\cdots=\xi_{km}=-1,\\ A_2 & \xi_{k1}=1,\xi_{k2}=0,\xi_{k3}=\cdots=\xi_{km}=-1,\\ A_3 & \xi_{k1}=\xi_{k2}=1,\xi+k3=0,\xi_{k4}=\ldots\xi_{km}=-1,\\ \vdots & \vdots \\ A_m & \xi_{k1}=\ldots\xi_{k,m-1}=1,\xi_{km}=0.\end{array}$$

It follows by definition that

$$\mathbb{E}_{\rho^{(r)}}\left[\log\left(\mathbb{P}[\xi_{k1},\ldots,\xi_{km},Z_k]\right)|Z_k=0\right] = \sum_{j=1}^{m}\log\left(\mathbb{P}_{\rho^{(r)}}[A_{kj}]\right)\cdot\mathbb{P}_{\rho^{(r)}}[A_{kj}|Z_k=0].$$

To evaluate the probability $\mathbb{P}_{\rho^{(r)}}[A_{kj}]$, note that A_{kj} happens if and only if

$$\sum_{i=1}^{j-1}\ell_i\rho_i < E_k \le \sum_{i=1}^{j}\ell_i\rho_i,$$

from which it follows that

$$\mathbb{P}_{\rho^{(r)}}[A_{kj}] = H\left(\sum_{i=1}^{j}\ell_i\rho_i\right) - H\left(\sum_{i=1}^{j-1}\ell_i\rho_i\right),$$

where we use the convention that $\sum_{i=1}^{0}\ell_i\rho_i=0$. Since $\sum_{j=1}^{m}\mathbb{P}[A_{kj}]=1-\mathbb{P}[Z=1]=1-H(L_k^t\rho)$, we deduce that

$$\mathbb{P}_{\rho^{(r)}}[A_{kj}|Z_k=0] = \frac{H\left(\sum_{i=1}^{j}\ell_i\rho_i^{(r)}\right)-H\left(\sum_{i=1}^{j-1}\ell_i\rho_i^{(r)}\right)}{1-H(L_k^t\rho^{(r)})}.$$

This leads us to write

$$\begin{aligned}\mathbb{E}_{\rho^{(r)}}\left[\log\left(\mathbb{P}_{\rho^{(r)}}[\xi_{k1},\ldots,\xi_{km},Z_k]\right)\middle|Z_k=0\right] &=\\ &\sum_{j=1}^{m}\log\left(H\left(\sum_{i=1}^{j}\ell_i\rho_i\right)-H\left(\sum_{i=1}^{j-1}\ell_i\rho_i\right)\right)\mathbb{P}_{\rho^{(r)}}[A_{kj}|Z_k=0].\end{aligned}$$

2.3.2 The maximization step

Some notational simplifications is possible if we define

$$S_{kj}=\sum_{i=1}^{j}\ell_{ki}\rho_i,\quad S_{k0}=0,$$

and

$$w_{kj}^{(r)} = \mathbb{P}_{\rho^{(r)}}[A_{kj}|Z_k = 0].$$

It then follows that

$$Q(\rho||\rho^{(r)}) \quad = \quad \sum_{k:Z_k=1} \log(1 - H(S_{km})) + \sum_{k:Z_k=0} \sum_{j=1}^{m} \log\left(H(S_{kj}) - H(S_{k,j-1})\right) w_{kj}^{(r)}.$$

The reason why people like the E-M algorithm, is that maximization of the original likelihood is hard but sometimes, maximizing $Q(\rho||\rho^{(r)})$ is easier. Unfortunately, this appears not to be the case in the considered problem[2]. Hence there are no advantages to consider the E-M algorithm in the current setting and one is likely to be better served to consider direct maximization of the likelihood function.

2.4 Direct Optimization

The E-M algorithm often reduces to making adjustements of one parameter at the time. While such "coordinate descent" is somewhat slower at reaching the minimum, it has the advantage of requiring less storage than other types of optimization methods. Managing storage requiremen of the optimization algorithm is important to enable scaling its applicability to millions of voxels. Here we discuss strategies for direct optimization of the likelihood function.

2.4.1 Newton Raphson

Newton Raphson maximizes a twice differenciable function f by iteratively calculating

$$x^{(r+1)} = x^{(r)} - \left(\nabla\nabla^t f(x^{(r)})\right)^{-1} \nabla f(x^{(r)}).$$

This procedure is both computationally expensive — it requires solving a $N \times N$ linear system — and requires large storage $O(N^2)$. That is, this procedure does not scale to the size of the problem we are interested in.

2.4.2 Coordinate descent Newton-Raphson

The numerical difficulties are lessened if the Hessian $\nabla\nabla^t f(x^{(r)})$ is sparse. For example, if the Hessian is diagonal, then the Newton-Raphson algorithm becomes equivalent to a Newton-Raphson coordinate descent method, that is one iteratively cycle through the parameter space, making each time just one NR adjustment. Find $x = (x_1, \cdots x_N \in R^N$ that maximizes the function $f(x)$, by iterating over all j, and by updating each x_j at a time as

$$x_{j+1} = x_j - \frac{f'(x_j)}{f''(x_j)}.$$

Using the loglikelihood function defined in (3), the first derivate of the loglikelihood is given by,

$$\frac{\partial \mathscr{L}(L_i^t\rho)}{\partial \rho_j} \quad = \quad \sum_{i=1}^{M} \frac{\partial}{\partial \rho_j} \left[Z_i \log(1 - H(L_i^t\rho)) + (1 - Z_i) \log H(L_i^t\rho)\right].$$

[2]Because we do not get a simple and easy algorithm, we sy by abuse of language, that the E-M algorithm does not work for our problem at hand.

We calculate

$$\begin{aligned}\frac{\partial}{\partial \rho_j}\left[(1-Z_i)\log H(L_i^t\rho) - Z_i\log(1-H(L_i^t\rho))\right] &= \ell_{ij}h(L_i^t\rho)\left(\frac{1-Z_i}{H(L_i^t\rho)} - \frac{Z_i}{1-H(L_i^t\rho)}\right)\\ &= \frac{\ell_{ij}h(L_i^t\rho)}{H(L_i^t\rho)(1-H(L_i^t\rho))}\left((1-Z_i)-H(L_i^t\rho)\right),\end{aligned}$$

where h is the density function of the particles' energy, that is $H'(x) = h(x)$. Hence,

$$\frac{\partial \mathscr{L}(L_i^t\rho)}{\partial \rho_j} = \sum_{i=1}^{M} \frac{\ell_{ij}h(L_i^t\rho)}{H(L_i^t\rho)(1-H(L_i^t\rho))}\left((1-Z_i)-H(L_i^t\rho)\right). \tag{4}$$

The second derivate of the loglikelihood is,

$$\begin{aligned}\frac{\partial^2 \mathscr{L}(L_i^t\rho)}{\partial \rho_j^2} &= -\sum_{i=1}^{M}\frac{(1-Z_i)\,\ell_{ij}^2}{H(L_i^t\rho)}\left(\frac{h^2(L_i^t\rho)}{H(L_i^t\rho)} - h'(L_i^t\rho)\right)\\ &\quad -\sum_{i=1}^{M}\frac{Z_i\,\ell_{ij}^2}{1-H(L_i^t\rho)}\left(\frac{h^2(L_i^t\rho)}{1-H(L_i^t\rho)} + h'(L_i^t\rho)\right),\end{aligned} \tag{5}$$

where $h'(\cdot)$ is the derivate of the density function. Finally, the *resistance* $\rho_j^{(k+1)}$ in the $k+1$ iteration will be calculated as,

$$\rho_j^{(k+1)} = \rho_j^{(k)} - \frac{\frac{\partial \mathscr{L}(L_i^t\rho^{(k)})}{\partial \rho_j^{(k)}}}{\frac{\partial^2 \mathscr{L}(L_i^t\rho^{(k)})}{\partial (\rho_j^{(k)})^2}}. \tag{6}$$

2.5 Implementation

The Newton-Raphson update rule (6) fails to be well defined in three instances. The first case is when $L_i^t\rho = 0$. In that case, both the first and second derivatives, see expressions (4) and (5) , are dividided by $0 = H(0)$. Since $L_i \geq 0$, this situation arises if the stopping density is zero along the entire path of the particle. Similarly, the second instance is when $L_i^t\rho$ is so large that $1 - H(L_i^t\rho) = 0$, and thus also the first and second derivatives are divided by zero. This happens for high energy particles that don't stop even though they may go through voxels with *high* stopping density. To resolve this problem, we propose the following minor modifications of the first and second derivatives: fix $\varepsilon > 0$ small, $C_1 > 0$ and $C_2 > 0$ large. then the first derivative can be expressed as

$$\begin{aligned}\frac{\partial \mathscr{L}(L_i^t\rho)}{\partial \rho_j} &= \sum_{i=1}^{M}\frac{\ell_{ij}h(L_i^t\rho)}{H(L_i^t\rho)}(1-Z_i) - \sum_{i=1}^{M}\frac{\ell_{ij}h(L_i^t\rho)}{1-H(L_i^t\rho)}Z_i\\ &\approx \sum_{\{i:Z_i=0\}}\ell_{ij}h(L_i^t\rho)\left(C_1 I_{\{L_i^t\rho<\varepsilon\}} + \frac{I_{\{L_i^t\rho\geq\varepsilon\}}}{H(L_i^t\rho)}\right)\\ &\quad -\sum_{\{i:Z_i=1\}}\ell_{ij}h(L_i^t\rho)\left(C_2 I_{\{L_i^t\rho>K\}} + \frac{I_{\{L_i^t\rho\leq K\}}}{1-H(L_i^t\rho)}\right).\end{aligned} \tag{7}$$

Similarly, the second derivative can be written as

$$\begin{aligned}\frac{\partial^2 \mathscr{L}(L_i^t\rho)}{\partial \rho_j^2} &= -\sum_{\{i:Z_i=0\}} \frac{\ell_{ij}^2}{H(L_i^t\rho)}\left(\frac{h^2(L_i^t\rho)}{H(L_i^t\rho)} - h'(L_i^t\rho)\right) \\ &\quad - \sum_{\{i:Z_i=1\}} \frac{\ell_{ij}^2}{1-H(L_i^t\rho)}\left(\frac{h^2(L_i^t\rho)}{1-H(L_i^t\rho)} + h'(L_i^t\rho)\right)\end{aligned} \tag{8}$$

which is approximately

$$\begin{aligned}\frac{\partial^2 \mathscr{L}(L_i^t\rho)}{\partial \rho_j^2} &\approx -\sum_{\{i:Z_i=0\}} C_1\,\ell_{ij}^2\left(C_1\,h^2(L_i^t\rho) - h'(L_i^t\rho)\right) I_{\{L_i^t\rho<\varepsilon\}} \\ &\quad - \sum_{\{i:Z_i=0\}} \frac{\ell_{ij}^2}{H(L_i^t\rho)}\left(\frac{h^2(L_i^t\rho)}{H(L_i^t\rho)} - h'(L_i^t\rho)\right) I_{\{L_i^t\rho\geq\varepsilon\}} \\ &\quad - \sum_{\{i:Z_i=1\}} C_2\,\ell_{ij}^2\left(C_2\,h^2(L_i^t\rho) + h'(L_i^t\rho)\right) I_{\{L_i^t\rho>K\}} \\ &\quad - \sum_{\{i:Z_i=1\}} \frac{\ell_{ij}^2}{1-H(L_i^t\rho)}\left(\frac{h^2(L_i^t\rho)}{1-H(L_i^t\rho)} + h'(L_i^t\rho)\right) I_{\{L_i^t\rho\leq K\}}.\end{aligned} \tag{9}$$

The third case is when the second derivate is zero. In that case, the log-likelihood is linear, and we propose to update the estimate using the rule

$$\rho_j^{k+1} = \begin{cases} \rho_j^k - \frac{\frac{\partial \mathscr{L}(L_i^t\rho^k)}{\partial \rho_j^k}}{\frac{\partial^2 \mathscr{L}(L_i^t\rho^k)}{\partial (\rho_j^k)^2}}. & \left|\frac{\partial^2 \mathscr{L}(L_i^t\rho^k)}{\partial (\rho_j^k)^2}\right| \geq \varepsilon \\ \rho_j^k(1-\Delta) & \left|\frac{\partial^2 \mathscr{L}(L_i^t\rho^k)}{\partial (\rho_j^k)^2}\right| < \varepsilon \text{ and } \frac{\partial \mathscr{L}(L_i^t\rho^k)}{\partial \rho_j^k} < 0 \\ \rho_j^k(1+\Delta) & \left|\frac{\partial^2 \mathscr{L}(L_i^t\rho^k)}{\partial (\rho_j^k)^2}\right| < \varepsilon \text{ and } \frac{\partial \mathscr{L}(L_i^t\rho^k)}{\partial \rho_j^k} > 0. \end{cases} \tag{10}$$

where the gradient and the second partial derivative are defined as in (7) and (9).

3 Simulations and Image Reconstruction assuming Exponential Energy Distribution

To apply this methodology, we need to know the distribution of the rays' incident energy. To test the methodology, for now, we assume that the energy distribution is exponential, and we produce simulations where the rays' energy are also exponential as described in section 3.1 . A more realistic distribution will be studied in section 4. The exponential distribution function, density and its derivate are defined for all $x > 0$ to be

$$\begin{aligned} H(x) &= P(X \leq x) = 1 - e^{-\lambda x}, && (11)\\ h(x) &= \lambda e^{-\lambda x}, && (12)\\ \frac{dh(x)}{dx} &= -\lambda^2 e^{-\lambda x} = -\lambda h(x), && (13) \end{aligned}$$

respectively. Substituting in equation (7), the first derivate of the the log-likelihood function becomes,

$$\begin{aligned} \frac{\partial \mathscr{L}(L_i^t\rho)}{\partial \rho_j} &= \sum_{\{i:Z_i=0\}} \ell_{ij} h(L_i^t\rho)\left(C I_{\{L_i^t\rho<\varepsilon\}} + \frac{I_{\{L_i^t\rho\geq\varepsilon\}}}{H(L_i^t\rho)}\right) - \sum_{\{i:Z_i=1\}} \frac{\ell_{ij} h(L_i^t\rho)}{1-H(L_i^t\rho)} \\ &= \sum_{\{i:Z_i=0\}} \ell_{ij} h(L_i^t\rho)\left(C I_{\{L_i^t\rho<\varepsilon\}} + \frac{I_{\{L_i^t\rho\geq\varepsilon\}}}{H(L_i^t\rho)}\right) - \sum_{\{i:Z_i=1\}} \lambda \ell_{ij} \qquad (14) \end{aligned}$$

Direct calculations of the second derivative reveals that the sum over all rays that go through ($Z_i = 1$) vanishes in the exponential case, because $h'(x) = -\lambda h(x)$, and therefore

$$\frac{h^2(L_i^t\rho)}{1-H(L_i^t\rho)} + h'(L_i^t\rho) = \frac{h(L_i^t\rho)}{1-H(L_i^t\rho)}\left(h(L_i^t\rho) - \lambda(1-H(L_i^t\rho))\right) = 0.$$

Thus the second derivative only depends on the stopped rays,

$$\begin{aligned} \frac{\partial^2 \mathscr{L}(L_i^t\rho)}{\partial \rho_j^2} &= -\sum_{\{i:Z_i=0\}} \frac{\ell_{ij}^2}{H(L_i^t\rho)}\left(\frac{h^2(L_i^t\rho)}{H(L_i^t\rho)} - h'(L_i^t\rho)\right) \\ &= -\sum_{\{i:Z_i=0\}} \frac{\ell_{ij}^2 h(L_i^t\rho)}{H^2(L_i^t\rho)}\left(h(L_i^t\rho) + \lambda H(L_i^t\rho)\right) \\ &= -\sum_{\{i:Z_i=0\}} \frac{\lambda\, \ell_{ij}^2 h(L_i^t\rho)}{H^2(L_i^t\rho)}, \end{aligned}$$

since $h(L_i^t\rho) + \lambda H(L_i^t\rho) = \lambda$. That is,

$$\frac{\partial^2 \mathscr{L}(L_i^t\rho)}{\partial \rho_j^2} \approx -\sum_{\{i:Z_i=0\}} \lambda\, \ell_{ij}^2 h(L_i^t\rho)\left(C^2 I_{\{L_i^t\rho<\varepsilon\}} + \frac{I_{\{L_i^t\rho\geq\varepsilon\}}}{H^2(L_i^t\rho)}\right). \qquad (15)$$

3.1 Simulations

We produced simulations of about 1 cubic meter volume, containing three $10cm^3$ objects of different density: aluminum (Al), iron (Fe), and tungsten (W). The energy distribution of the incident particles was assumed to be exponential with mean 3GeV (i.e. $P(E < x) = 1 - e^{-x/3}$). The energy loss in this simulations is assumed to be 2 MeV/g/cm. Each simulation had about 170,000 rays. To have a clean stopping signal we produced simulations without any scattering of the particles. In later numerical experiments, we also produced more realistic simulations, that included scattering of charged particles.

The image reconstruction of both simulations was done using a coordinate descent Newton-Raphson method to maximize the log-likelihood function as described in the previous section. We voxelized the volume in $10cm^3$ voxels, namely $11 \times 11 \times 9 = 1089$ voxels, and calculated the path of each particle through the volume. For the simulation with scattering the path of each ray is calculated as the path going through the line defined by the incident point and angle up to the intersection with the line defined by the outgoing point and angle.

The initial reconstructions took about an hour, so we were concerned that long computing time would prevent us from making numerous reconstructions as needed for ROC curves based performance analysis. We optimized out MatLab code with a goal to make the single scene reconstruction in less than a minute. The optimized code runs in 48 seconds; this includes reading the files, cleaning and formatting the data appropriately, running the reconstruction and producing the plots. While in the near future we are going to switch to more complicated and larger scenes, we expect computing time not to be a large hindrance at that point. We will however continue to monitor it for make sure that our ability to make serial simulations is not impeded.

3.2 Results

Scene: "Aluminum, Iron, Tungsten". For this simulations, the actual *resistance* in each voxel is given by the element's volume density times the energy loss per traversed centimeter, in this case 2 MeV/g/cm,

$$
\begin{aligned}
\rho_{\mathrm{W}} &= 2\frac{MeV}{g/cm} \times 19.3\frac{g}{cm^3} = 38.60\frac{MeV}{cm} \\
\rho_{\mathrm{Fe}} &= 2\frac{MeV}{g/cm} \times 7.87\frac{g}{cm^3} = 15.80\frac{MeV}{cm} \\
\rho_{\mathrm{Al}} &= 2\frac{MeV}{g/cm} \times 2.68\frac{g}{cm^3} = 5.38\frac{MeV}{cm} \\
\rho_{\mathrm{Air}} &= 2\frac{MeV}{g/cm} \times 0.0012\frac{g}{cm^3} = 0.0024\frac{MeV}{cm}
\end{aligned}
$$

Note that according to the particle data book, the energy loss per centimeter is not 2 MeV/(g/cm), but varies for these three materials, namely Tungsten 1.145 MeV/g/cm, Iron 1.451MeV/g/cm, and Aluminum 1.615 MeV/g/cm. [3]

Our current reconstruction methods are optimized for nuclear materials detection. For that task, an overestimation of the signal is not a problem, because the threatening material is still detected.

[3] If GEANT4 uses these numbers, then contrast between these three materials would be reduced and the "true" values would be different. We should check to see what results we get with GEANT4 simulations.

The situation is different for explosives detection, because both underestimation of the signal (e.g., misidentification of a TNT block as a round of cheese), and overestimation of the signal (misidentification of TNT block as a car battery) both lead to a decrease of detection efficiency. For this project, we need to understand, how closely our estimated values are to the true material parameters. We need to evaluate our current methods and decide which one has the optimal performance for our application. Figure 2 shows the stopping image reconstruction of three blocks of different materials for both models: excluding and including scattering. Reconstructed values (energy loss, proportional to the material density) are close to the simulated ones, confirming the validity of our reconstruction methods. Large signal spread is noticeable when adding scattering to the simulation. Reconstructed values for central voxels show some leakage of the signal to the neighboring voxels.

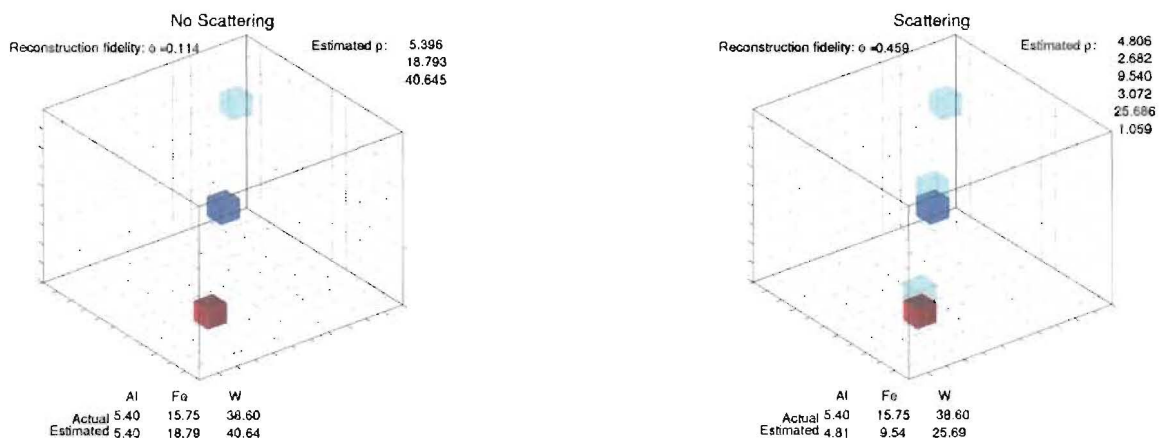

Figure 2: Stopping Reconstruction of three materials: aluminium, iron, and tungsten.

4 Soft Cosmic Particles' Energy Distribution

Given that the reconstruction algorithm based on maximum likelihood seems reasonable assuming the cosmic rays' energy distribution is exponential, we will now try to investigate if we can find a parametric distribution that fits better the actual rays' energy distribution.

The soft particles we deal with are typically a combination of electrons and muons. Their proportions on any given location and point in time, seem to depend on many factors, particularly, they depend on the altitude, and the weather conditions, *e.g.* if it is cloudy, rainy or if their is a fair sky. At sea level typically there are about 70% electrons and 30% muons, while at higher altitudes, *e.g.* in Los Alamos, NM, which is located at 7,200 ft, the muons and electrons' proportion seems to be equal.

We generated 10 million electrons and 10 million muons from tables produced using empirical observations, and anlayze first electrons and muons separately by drawing the corresponding histograms. We considered various well known densities, and plotted the ones that seem closer to the observed energy histogram, namely, the Gamma, Inverse Gamma, Pareto and Log-Normal densitites, as seen in figure (3).

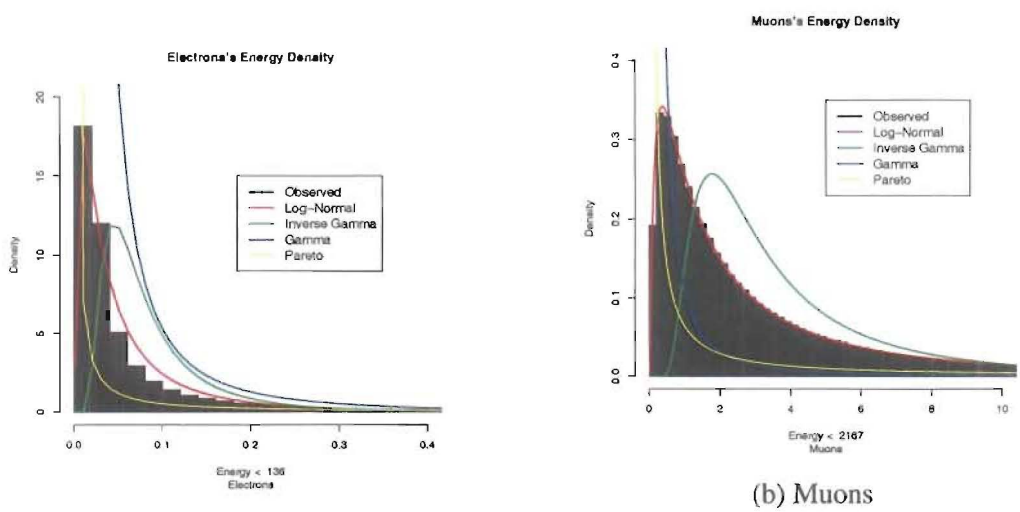

(a) Electrons

(b) Muons

Figure 3: Energy Density

The log-normal density is the closest to the electrons energy density, and it particularly fits the muons' energy density rather well. Although we are mainly interested in lower energy particles, that are more likely to stop, figures (4) and (5) provide a closer look at the tails. Recall that a log-normal random variable, is such that its logarithm has normal or gaussian distribution, namely for $x > 0$,

$$f(x;\mu,\sigma) = \frac{1}{x\sigma\sqrt{2\pi}} e^{-\frac{(\ln(x)-\mu)^2}{2\sigma^2}}. \tag{16}$$

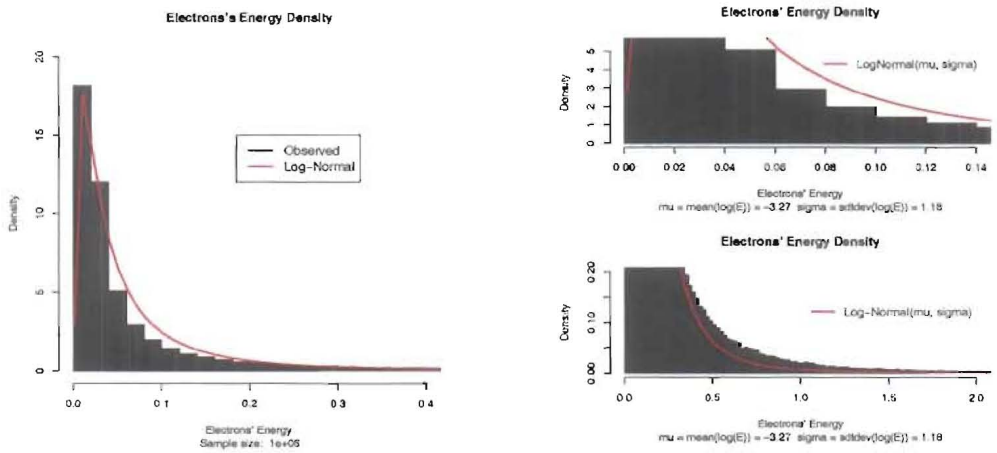

Figure 4: A closer look to the Electrons' Energy Density

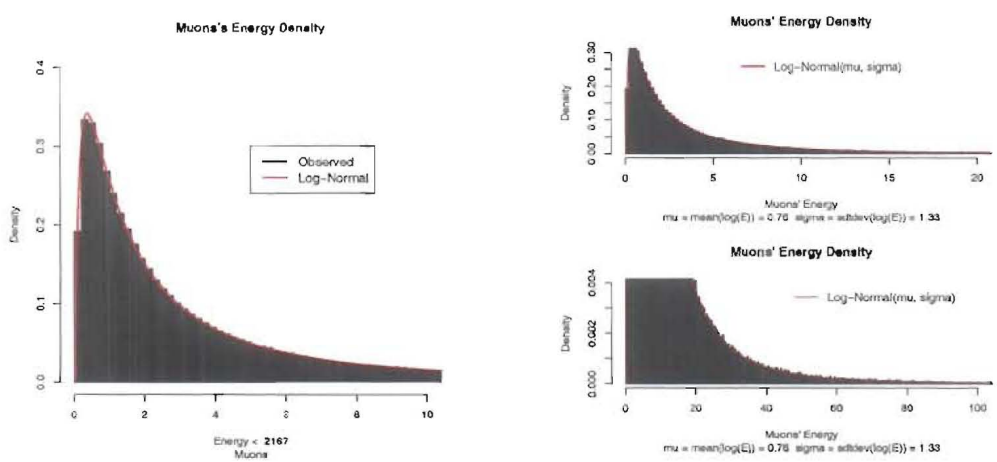

Figure 5: A closer look to the Muons' Energy Density

Next, we pull all the particles together, with an equal proportions of electrons and muons, and plot a mixture of the log-normals that fitted the electrons and muons' density, this is,

$$\alpha f(x, \widehat{\mu}_{elect}, \widehat{\sigma}_{elect}) + (1-\alpha) f(x, \widehat{\mu}_{muons}, \widehat{\sigma}_{muons}) \tag{17}$$

where the maximum likelihood estimates are $\widehat{\mu}_{elect} = -3.27, \widehat{\sigma}_{elect} = 1.18$, $\widehat{\mu}_{muons} = 0.76, \widehat{\sigma}_{muons} = 1.33$, and $\alpha = \frac{1}{2}$.

Figures (6) and (7) show that this mixture of log-normals is a fairly good approximation to the soft cosmic particles' energy.

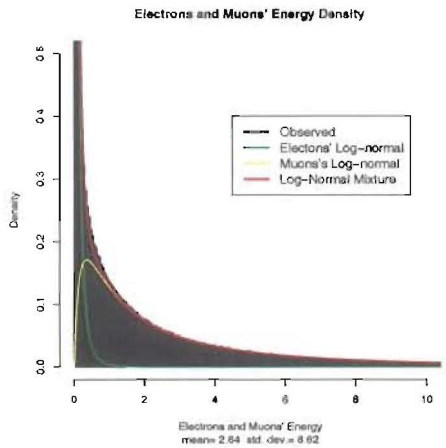

Figure 6: Soft Cosmic Particles Energy Density

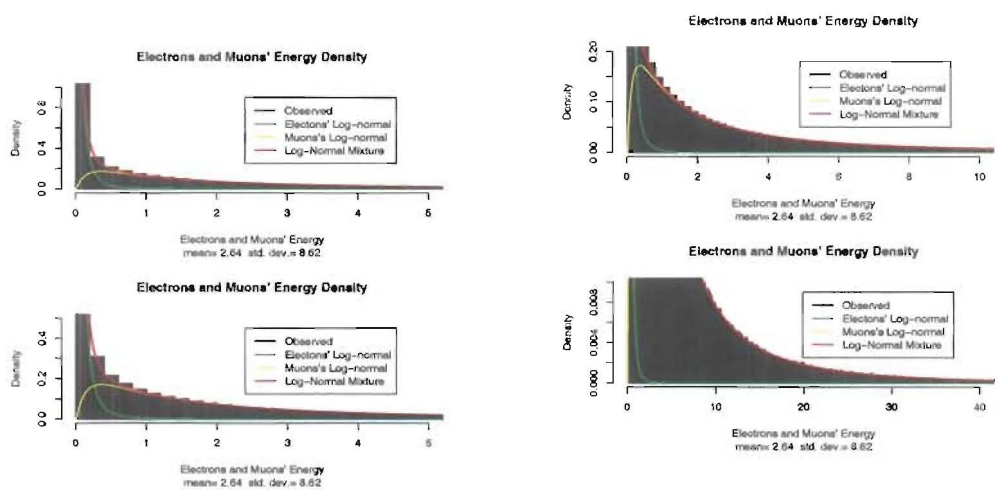

Figure 7: A closer look to the Soft Cosmic Particles Energy Density

5 Simulations and Image Reconstruction using a Mixture of Log-normals

To maximixe the log-likelihood function defined in (3), we need the lognormal distribution, density and its first derivate. The distribution function is given by

$$F(x,\alpha,\mu,\sigma) = \int_0^x f(y,\mu,\sigma)dy = \frac{1}{2}+\frac{1}{2}\operatorname{erf}\left(\frac{\ln(x)-\mu}{\sigma\sqrt{2}}\right) \tag{18}$$

where erf is the error function defined as $\operatorname{erf}(x) = \frac{2}{\sqrt{\pi}}\int_0^x e^{-t^2}dt$, and f is the density,

$$f(x;\mu,\sigma) = \frac{1}{x\sigma\sqrt{2\pi}}e^{-\frac{(\ln(x)-\mu)^2}{2\sigma^2}}. \tag{19}$$

Finally the first derivate of the density is,

$$\frac{df(x;\mu,\sigma)}{dx} = -\frac{1}{x}f(x;\mu,\sigma)\left(1+\frac{\ln(x)-\mu}{\sigma^2}\right). \tag{20}$$

The corresponding distribution, density and first derivate of the mixture of log-normals, is just the convex combination of the corresponding functions given in (18) to (20)

$$\begin{aligned}
H(x,\alpha,\mu_{elect},\sigma_{elect},\mu_{muons},\sigma_{muons},) &= \alpha F(x,\alpha,\mu_{elect},\sigma_{elect})+(1-\alpha)F(x,\alpha,\mu_{muons},\sigma_{muons}),\\
h(x,\alpha,\mu_{elect},\sigma_{elect},\mu_{muons},\sigma_{muons},) &= \alpha f(x,\alpha,\mu_{elect},\sigma_{elect})+(1-\alpha)f(x,\alpha,\mu_{muons},\sigma_{muons}),\\
\frac{dh(x,\alpha,\mu_{elect},\sigma_{elect},\mu_{muons},\sigma_{muons})}{dx} &= \alpha\frac{df(x,\alpha,\mu_{elect},\sigma_{elect})}{dx}+(1-\alpha)\frac{df(x,\alpha,\mu_{muons},\sigma_{muons})}{dx}.
\end{aligned}$$

We implement exactly formulas (4) and (5) since when substituting H, h and $\frac{dh}{dx}$ nothing simplifies.

5.1 Simulations and Results

We simulated the same scene as described in section 3.1, this is about a one cubic meter volume containing three 10 cm^3 objects: aluminium, iron and tungsten. The energy loss distribution was assumed to be an $\alpha-$mixture of lognormals as described in the previous section, where α is the proportion of muons. We varied the proportions of muons and electrons: i) 100% muons (with $\alpha = 1$), ii) 100 % electrons ($\alpha = 0$), iii) the same proportions of muons and electrons ($\alpha = 50\%$), and iv) 70% muons and 30% electrons. The energy loss in the simulation is assumed to be 2 MeV/g/cm. We produced simulations with about 161K rays and with about twice as many rays 322K, and again we produced simualtions without and with scattering. For each of the scenarios we performed 10 simulations. The results are summarized in figures 9 to 12. The simulation code was written in Matlab.

The stopping reconstructions for the simulations using only muons (figure 9) look very reasonable, with obvious improvements by doubling the exposure times, and smaller standard deviations for the simulations done with no scattering. Similar results are obtained when only using electrons (10) , with two main differences: first note that when assuming no scattering, the electrons seem to be more useful for identifying lower density materials like iron and aluminium, then higher density materials like tungsten, where the stopping density is somewhat underestimated; and second, adding scattering

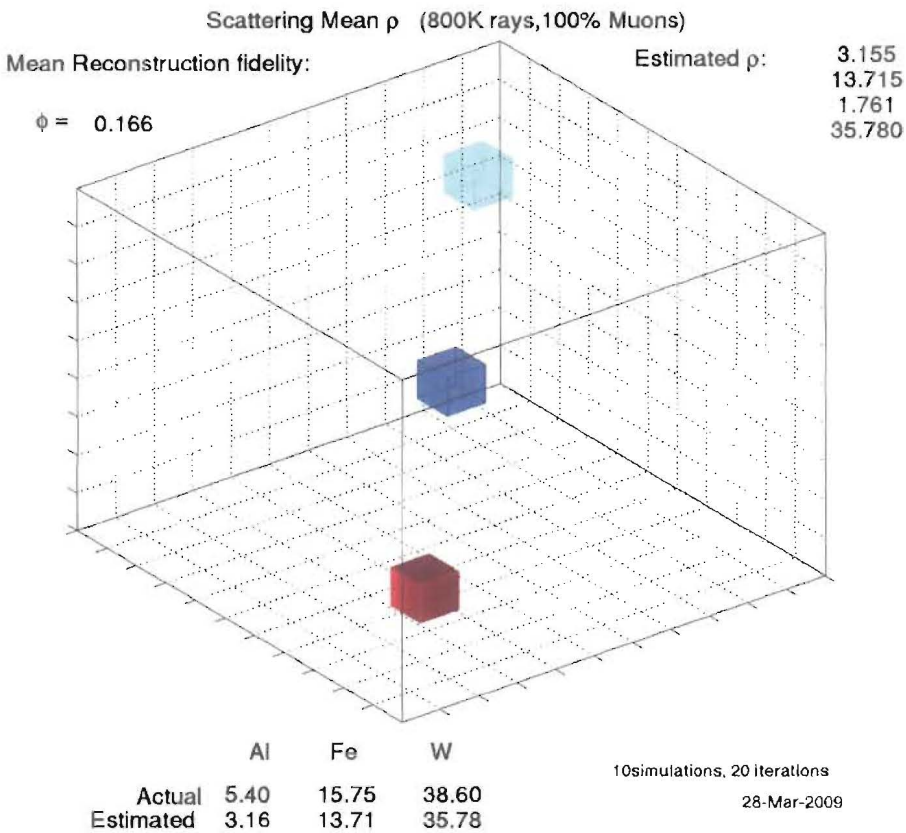

Figure 8: Image reconstruction. Scene: Tungsten, iron, and aluminium

makes the previous situation much worse. Electrons may scatter more when hitting higher density material, and thus our estimation of the rays' paths needs to be significantly improved. These effects get carried over when mixing electrons and muons (11 and 12).

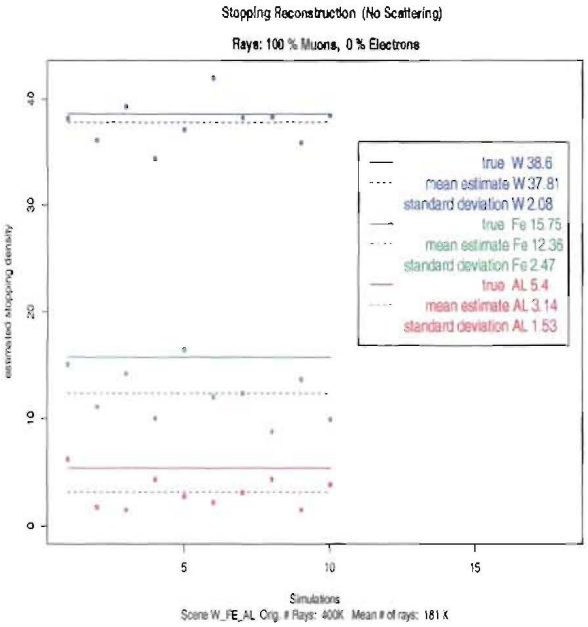

(a) No Scattering, 181K rays

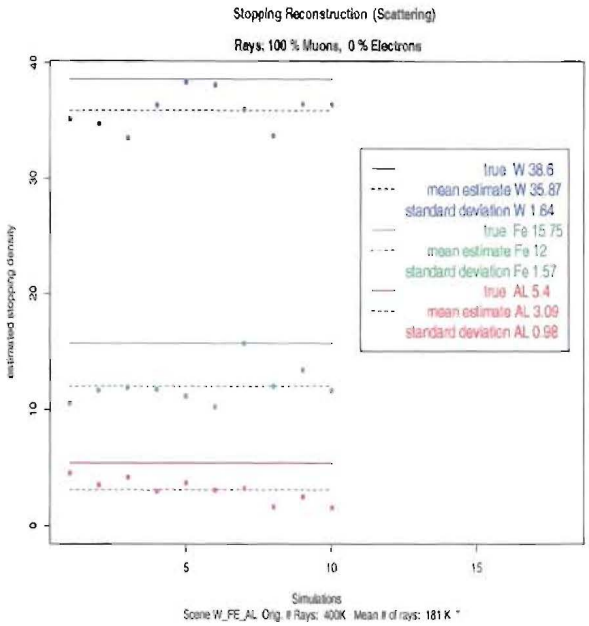

(b) Scattering, 181K rays

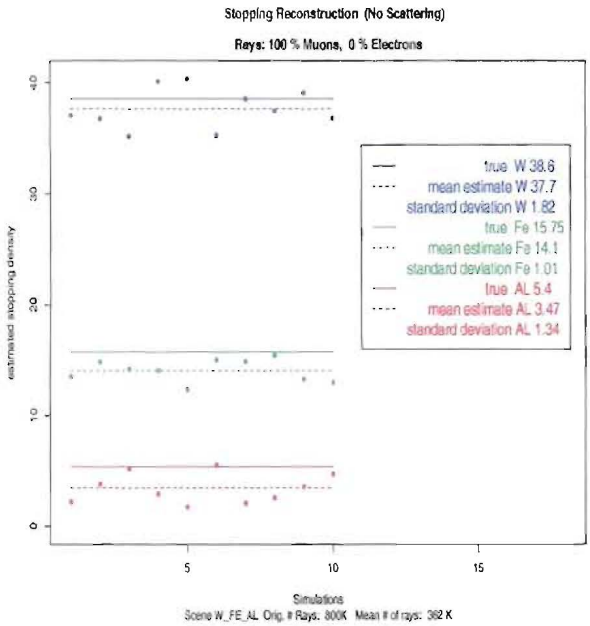

(a) No scattering, 362K rays

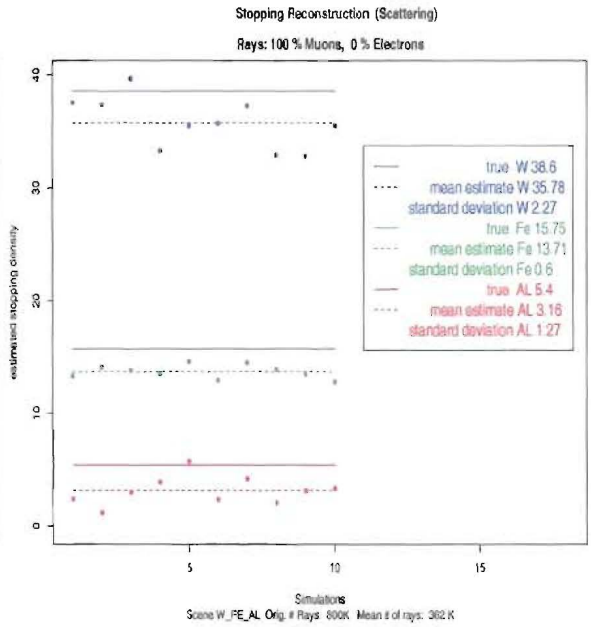

(b) Scattering, 362K rays

Figure 9: Simulations with 100% Muons. Scene: Aluminium, iron and tungsten.

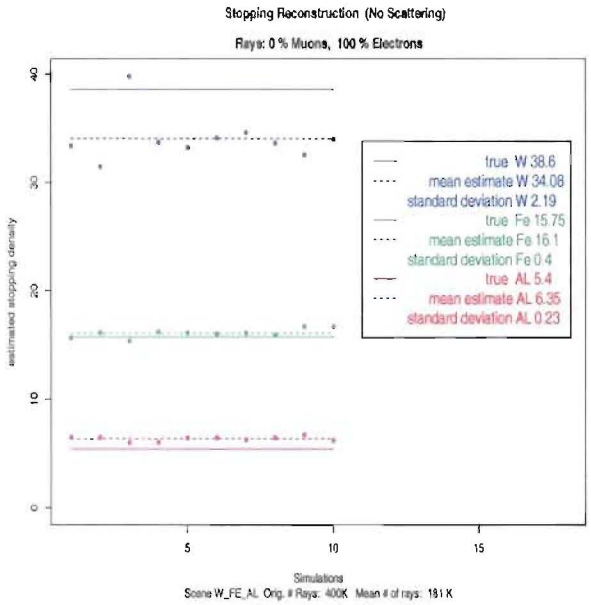

(a) No Scattering, 181K rays

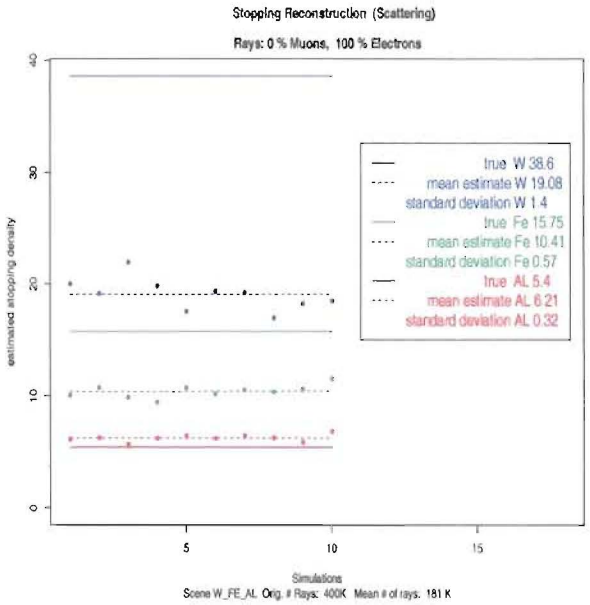

(b) Scattering, 181K rays

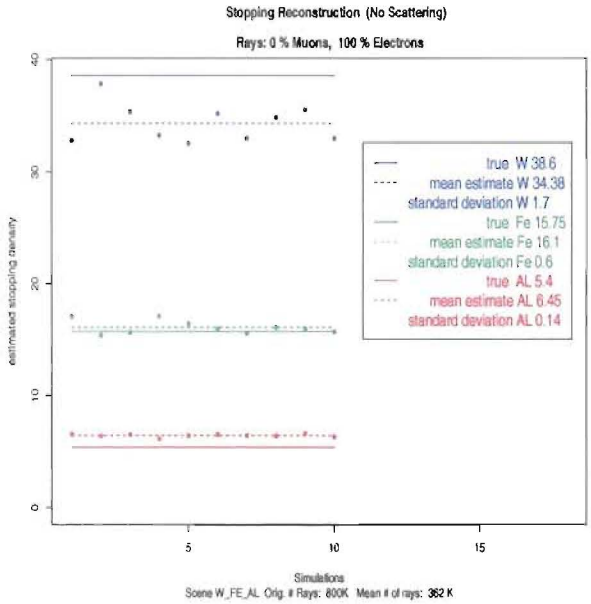

(a) No scattering, 362K rays

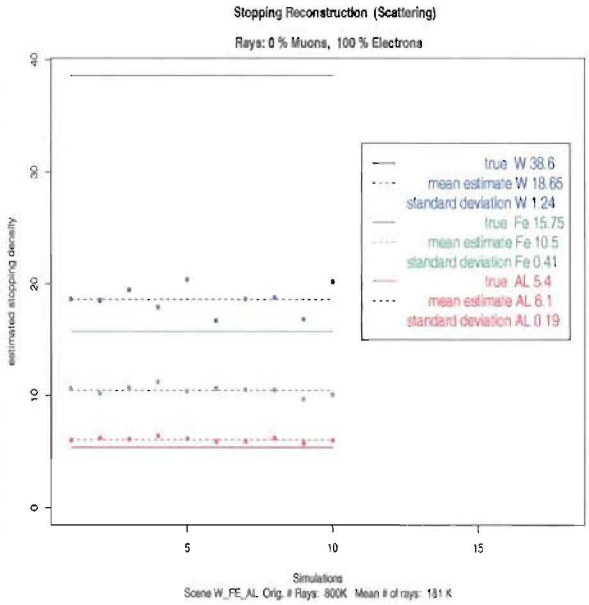

(b) Scattering, 362K rays

Figure 10: Simulations with 100% Electrons. Scene: Aluminium, iron and tungsten.

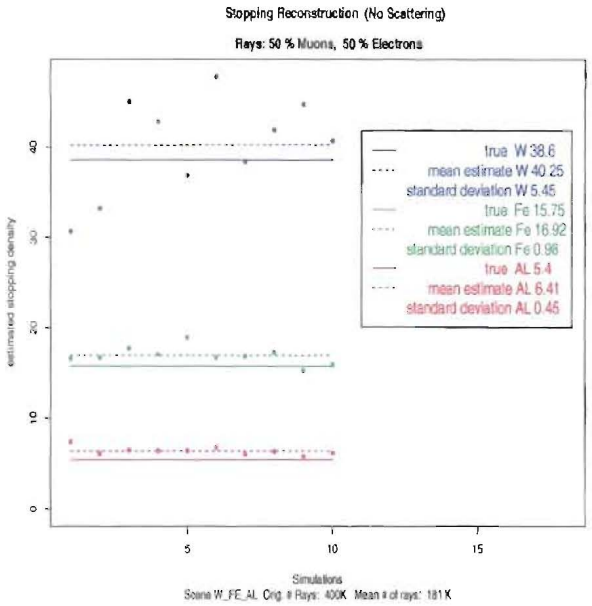

(a) No Scattering, 181K rays

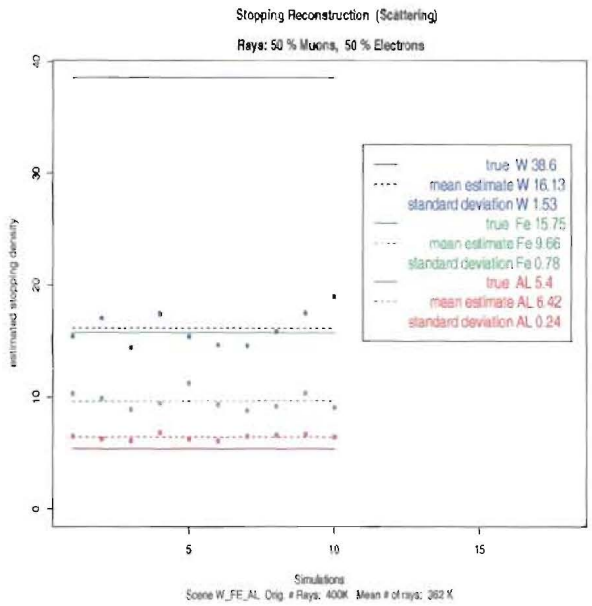

(b) Scattering, 181K rays

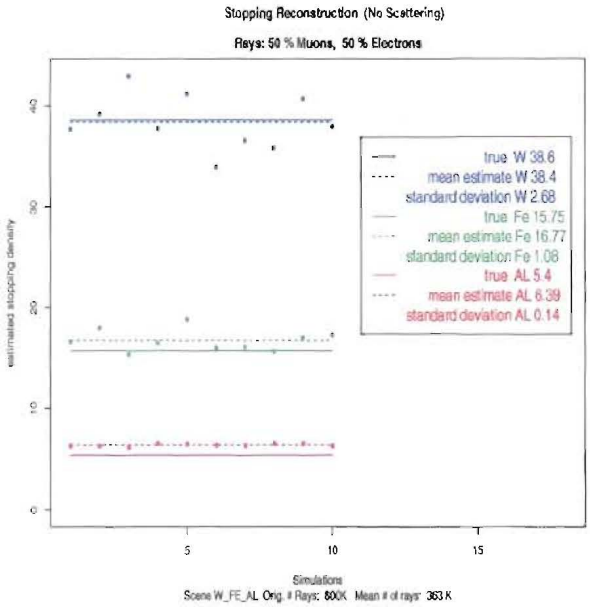

(a) No scattering, 362K rays

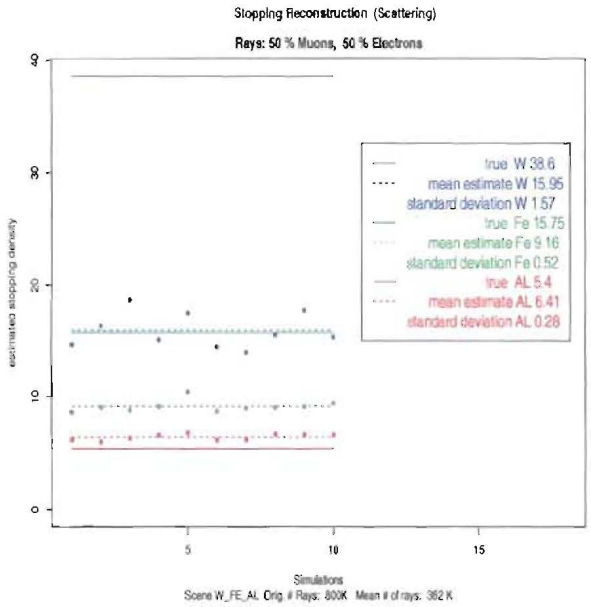

(b) Scattering, 362K rays

Figure 11: Simulations with 50% Muons and 50% Electrons. Scene: Aluminium, iron and tungsten.

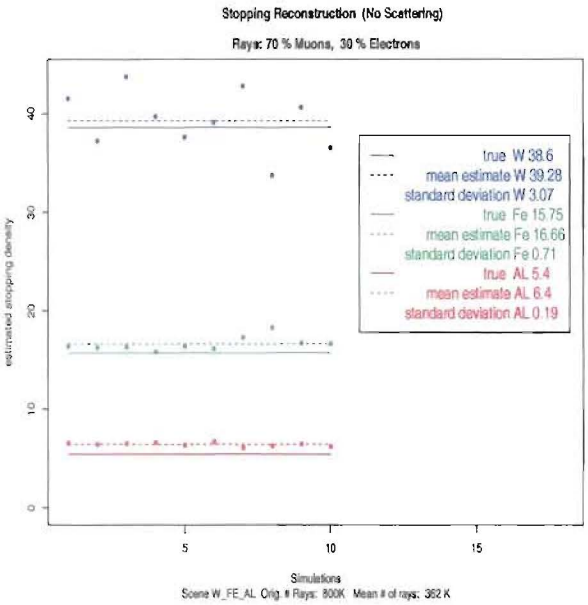

(a) No scattering, 362K rays

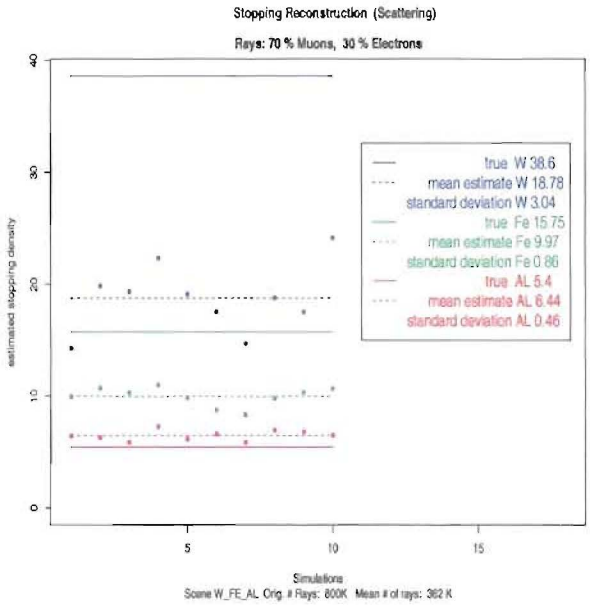

(b) Scattering, 362K rays

Figure 12: Simulations with 70% Muons and 30% Electrons. Scene: Aluminium, iron and tungsten

To verify if the position of the objects matters or not, we run the set of simulations with the twist that aluminium and tungsten switched places (see figures 14). Again, we find that electrons do a better job at identifying lower density materials like aluminium and iron, than higher density materials like tungsten. Interestingly, when including scattering in the simulation, even though the stopping density of tungsten is still underestimated, it improved considerably (compare figures 11and 14).

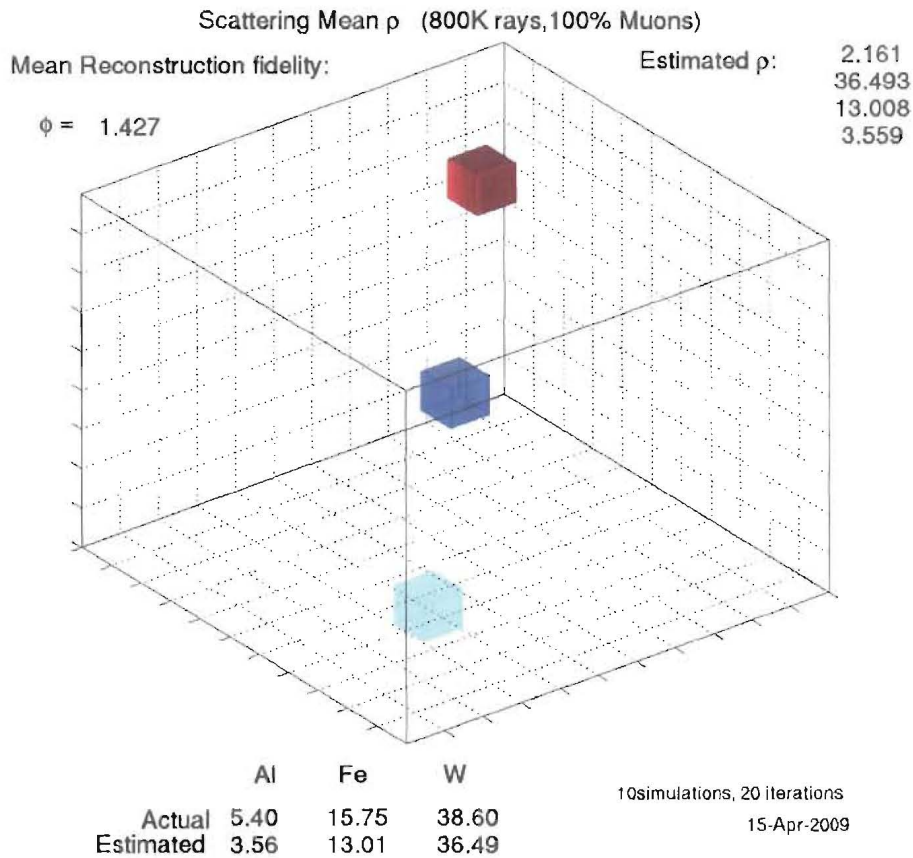

Figure 13: Image reconstruction. Scene: Tungsten, iron, and aluminium

100% Muons

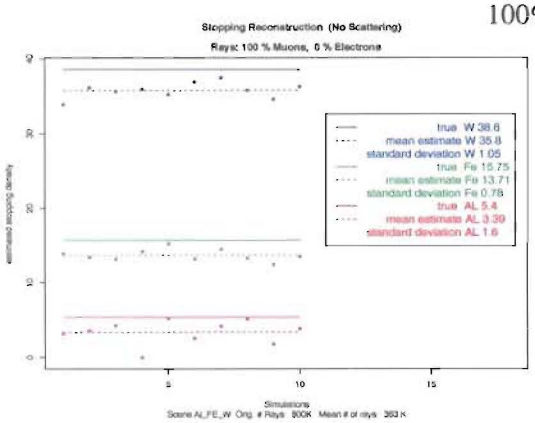

(a) No Scattering, 362K rays

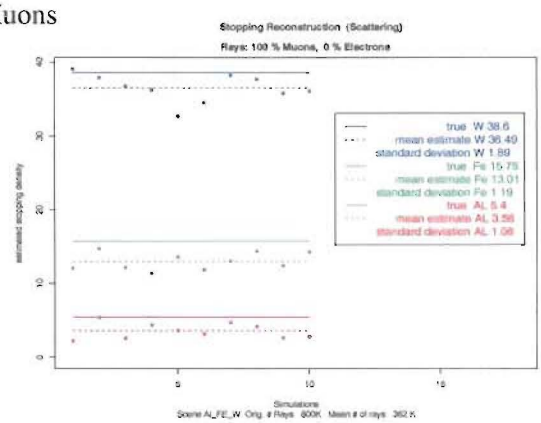

(b) Scattering, 362K rays

100% Electrons

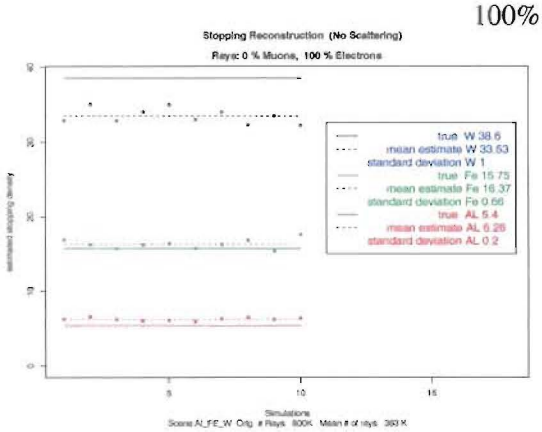

(a) No scattering, 362K rays

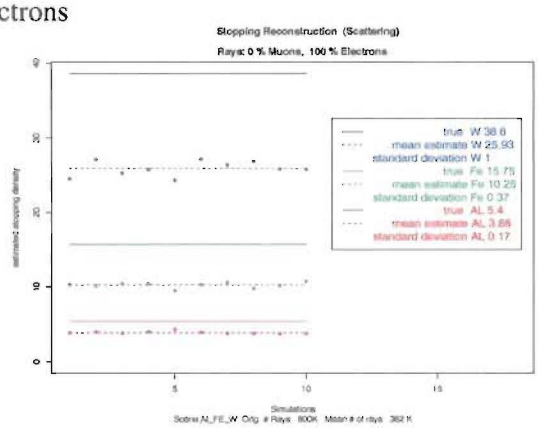

(b) Scattering, 362K rays

50% Muons and 50% Electrons

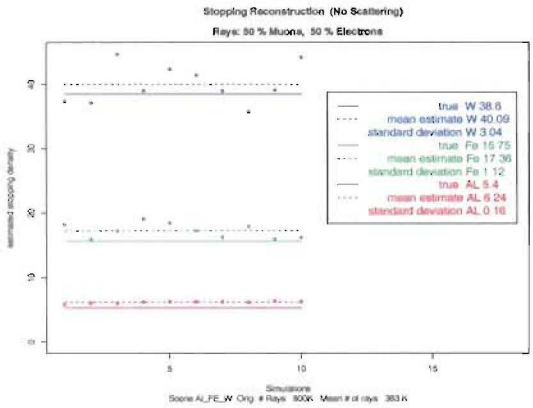

(a) No scattering, 362K rays

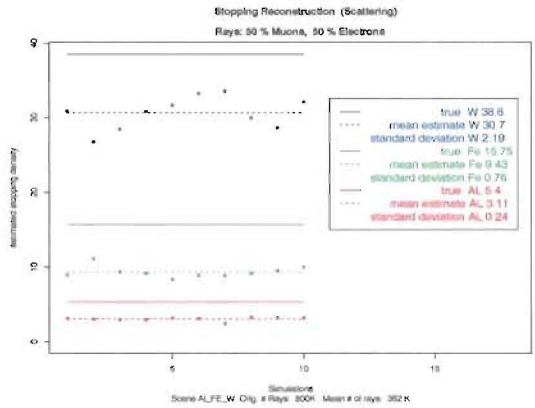

(b) Scattering, 362K rays

Figure 14: Flipped scene: Tungsten, iron and aluminium

6 Geant Simulations

Having tested the methodology to identify lower Z-material using the more simple Matlab simulations, we created simulations with Geant 4 that uses more realistic particles' behavior, that include the incident energy, the energy loss, and the scattering. The landscape was kept simple with four $10cm^3$ cubes of low-medium Z density material, namely iron, aluminium, TNT and water. In each experiment we used an exposure time of one minute, with a mixture of particles of 50% muons and 50% electrons, and the experiment was repeated 100 times.

We apply our algorithm as described in section 5 assuming the particles' incident energy is a mixture of log-normals. Figure 15 shows the mean image reconstruction over all 100 simulations that uses the mean estimated stopping density in each voxel. It is surprising how well the algorithm can identify the presence of objects in the different voxels, and on average it also does a very good job at distinguishing among the different materials. Unfortunately, when taking a closer look at individual simulations (see figure 16), it is obvious that it is not always clear that one can distinguish among the different materials. This is confirmed by looking at the boxplots in figure 17 that show the overlap of the empirical estimated stopping densities distribution of the different materials.

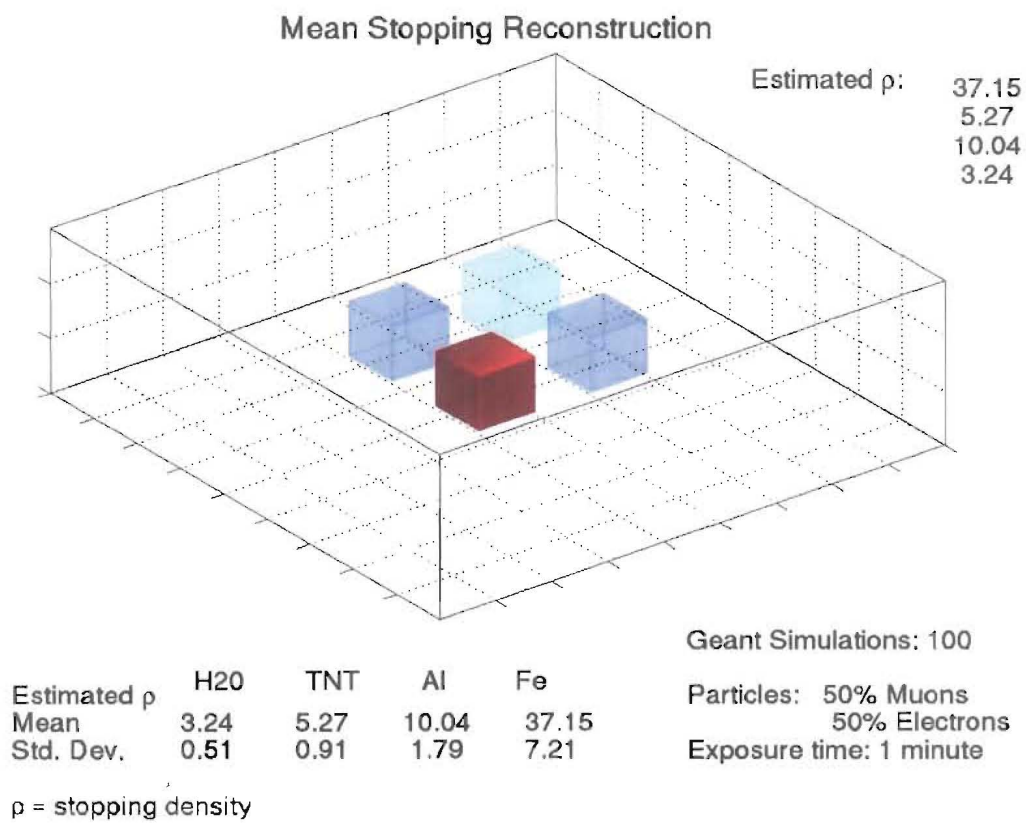

Figure 15: Image stopping reconstruction of water, TNT, aluminium, and iron with 1 minute exposure time

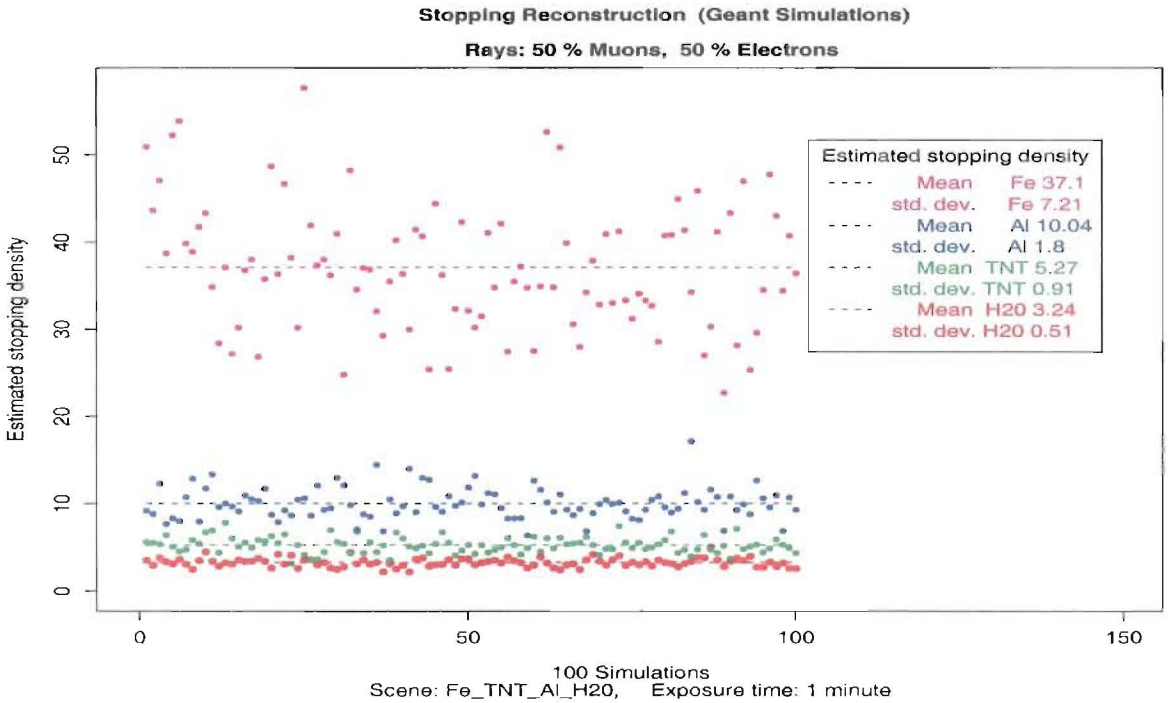

(a) Scene: Water, TNT, aluminium, and iron. 1 minute exposure time

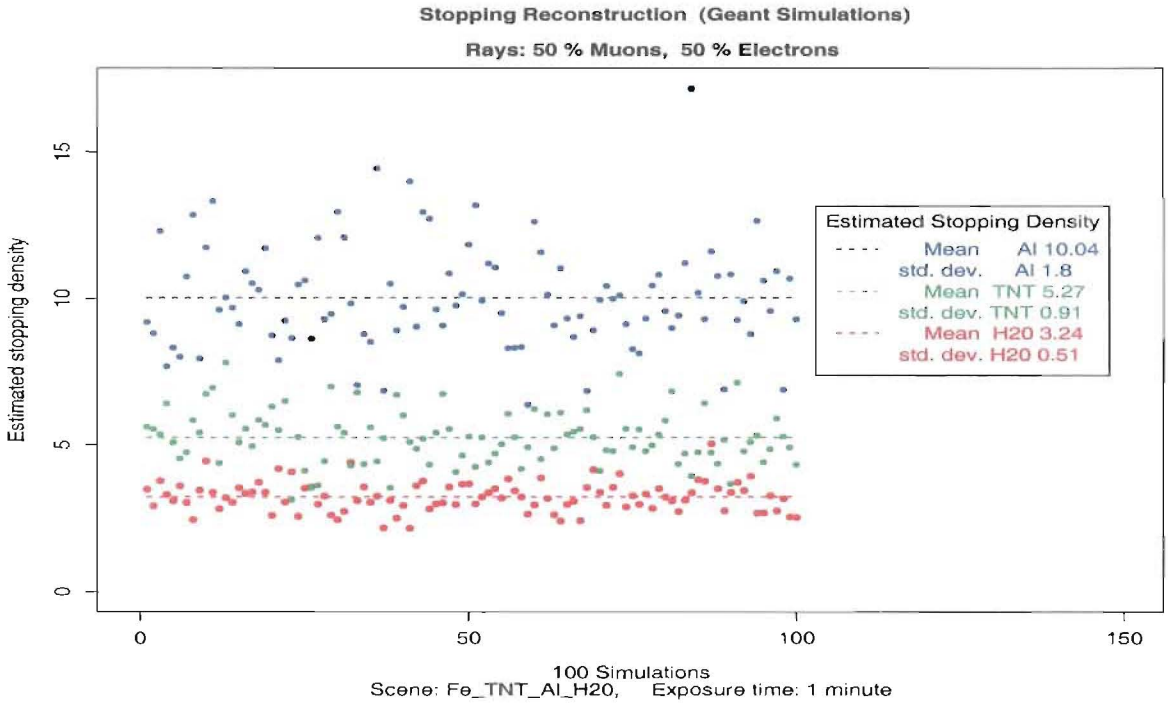

(b) Zooming in: Water, TNT, and aluminium. 1 minute exposure time

Figure 16: Estimated stopping densities estimates of Geant Simulations

Boxplots illustrate differences between empirical distributions without making assumtions on the underlying statistical distribution. A boxplot is construted using the lower and upper quartiles (end of the box), the median (the line inside the box) and the samples minimum and maximum (whiskers). Thus the lenght of the box is the interquartile range (IQR). Any point that lies 1.5 times the IQR from aboxe the third quartile or below the first quartile is considered an outlier and is individually displayed with a point.

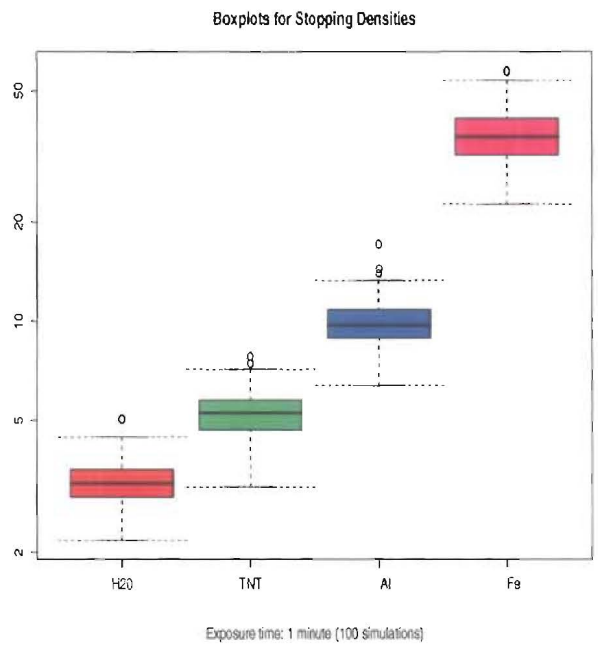

Figure 17: Boxplots of estimated stopping densities of water, TNT, aluminium, and iron with 1 minute exposure time

The inability of the algorithm to clearly distinguish between different materials is resolved by doubling the exposure time. The stopping reconstruction was performed using 50 simulations of the same scene (four $10cm^3$ of water, TNT, aluminium, and iron) with an exposure time of 2 minutes each. Figures 18 and 19 compare the stopping reconstruction scattering plots and boxplots with one and two minutes exposures. The two minute exposure plots clearly show the material separation.

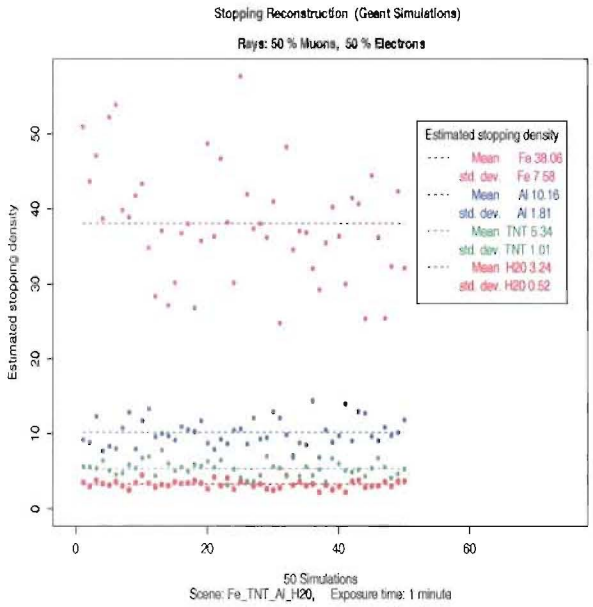

(a) Exposure time: 1 minute

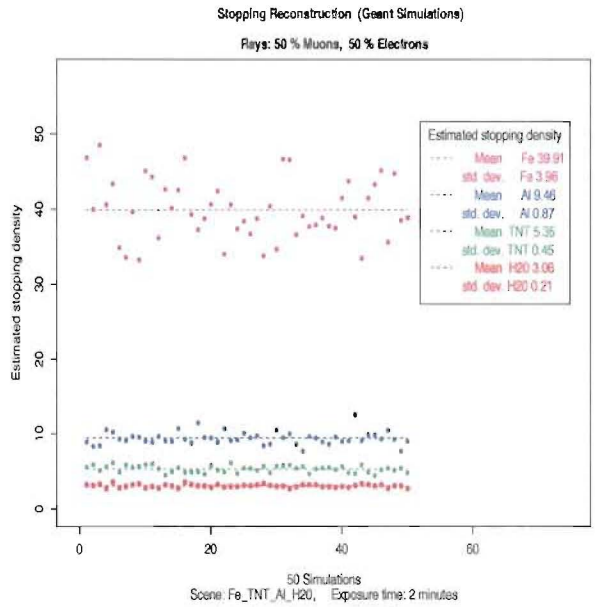

(b) Exposure time: 2 minutes

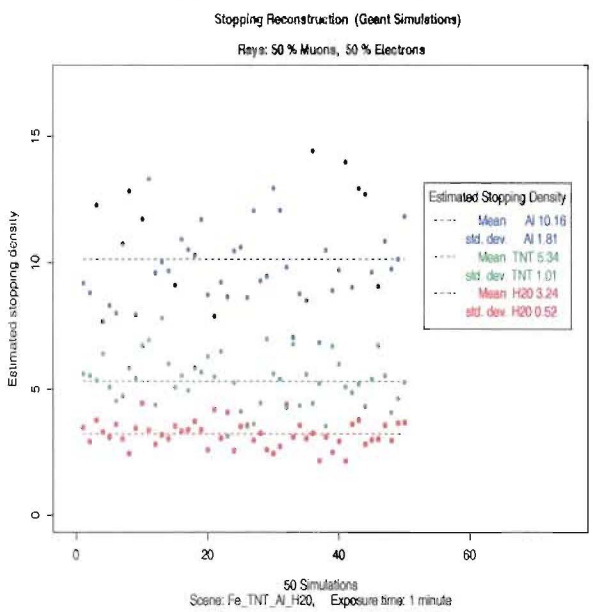

(a) Exposure time: 1 minute

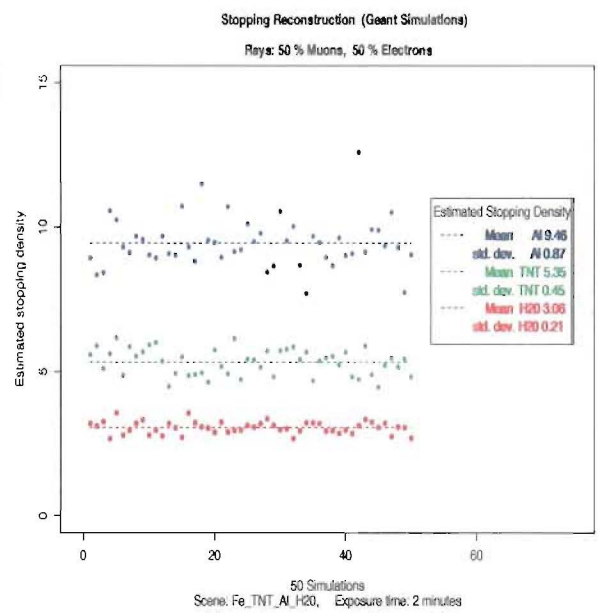

(b) Exposure time: 2 minutes

Figure 18: Estimated stopping densities of water, TNT, aluminium, and iron. 50 simulations.

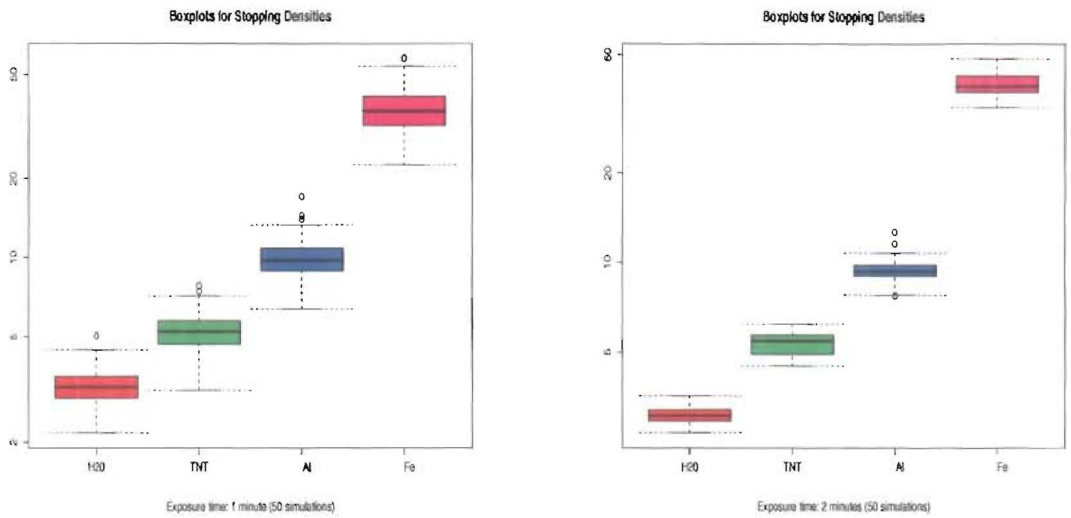

(a) Exposure time: 1 minute

(b) Exposure time: 2 minutes

Figure 19: Estimtaed stopping densities of water, aluminium, TNT, and iron. 50 simulations.

Finally, figure 20 shows the mean image reconstruction using the fifty 2 minutes simulations.

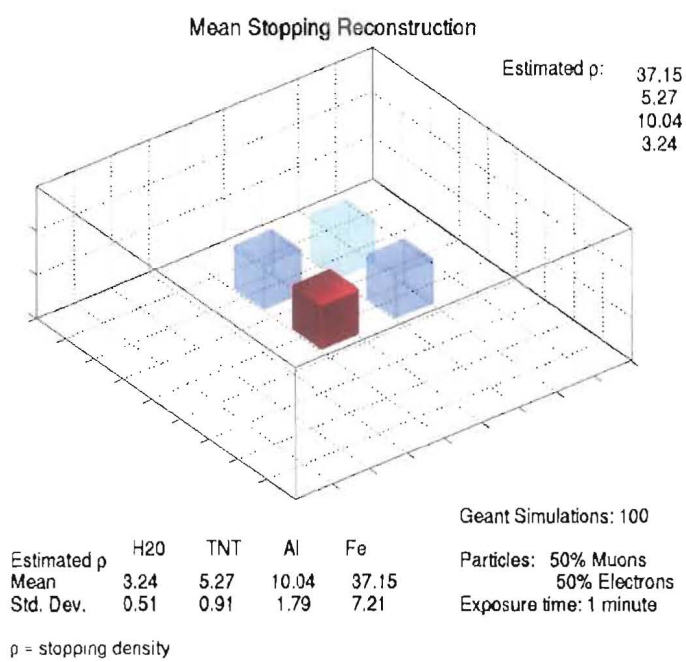

Figure 20: Image stopping reconstruction of water, TNT, aluminium, and iron with 2 minutes exposure time

7 Conclusion

Analysis of stopped charged particles provide a complimentary view to scattering tomography and helps resolve medium and low Z materials. Combining scattered and stopped particles has the potential of increasing the dynamic range in the reconstruction at little or no costs in terms of exposure times and complexity of the measurement apparatus. This opens the door for a broader range of application for passive tomography, with possible applications ranging from the detection of explosives to passive imaging of buildings and dams.

References

[1] Atomic and Nuclear Propeties of materials. http://pdg.lbl.gov/2007/reviews/atomicrpp.pdf

[2] Borozdin, K., On the Stopping of electrons in matter and its correlation with scattering of muons in the same object, Los Alamos National aboratory, July, 2006.

[3] Borozdin, K. G.E. Hogan, C. Morris, W. C. Priedhorsky, A. Saunders, L.J. Schultz, M.E. Teasdale, Surveillance: Radiographic imaging with cosmic-ray muons, Nature **422**, 277, March, 2003.

[4] Cuéllar, L. Information in Stopped Particles, Los Alamos National Laboratory, October 2008.

[5] Morris, C. Soft Cosmic Ray Radiography, Los Alamos National Laboratory, August, 2008.

[6] Schulz, L., K. Borozdin, A. Fraser, A. Klimenko, N. Hengartner, C. Morris, C. Orum, M. Sossong. Statistical Tomographic Reconstruction for Cosmic Ray Muon Tomography, IEEE transactions on Image Processing, **16**, 8, pp. 1985-1993, August, 2007.

[7] Schulz, L., G. Blanpied, K., Borozdin, A. Fraser, A. Klimenko, N. Hengartner, C. Morris, C. Orum, M. Sossong. ML/EM Reconstruction for Cosmic Ray Muon Tomography, IEEE Nuclear Science Symposium Conference Record, **8**, pp 2574-2578, October, 2006